Optimizing The Activity of Nano-needle Structured WO_3 Photoanodes for Solar Water Splitting – Direct Synthesis *Via* Chemical Vapor Deposition

Andreas Kafizas,[a] Laia Francàs,[a] Carlos Sotelo-Vazquez,[b] Min Ling,[b] Yaomin Li,[b] Emily Glover,[b] Liam McCafferty,[b] Chris Blackman,[b] Jawwad Darr [b] and Ivan Parkin[b]*

[a] Department of Chemistry, Imperial College London, SW7 2AZ

[b] Department of Chemistry, University College London, WC1H 0AJ

ABSTRACT: Solar water splitting is a promising solution for the renewable production of hydrogen as an energy vector. To date, complex or patterned photoelectrodes have shown the highest water splitting efficiencies, but lack scalable routes for commercial scale-up. In this article, we report a direct and scalable chemical vapor deposition (CVD) route at atmospheric pressure, for a single step fabrication of complex nano-needle structured WO_3 photoanodes. Using a systematic approach, the nanostructure was engineered to find the conditions that result in optimal water splitting. The nanostructured materials adopted a monoclinic γ-WO_3 structure and were highly oriented in the (002) plane, with the nano-needle structures stacking perpendicular to the FTO substrate. The WO_3 photoanode that showed the highest water splitting

activity was composed of a ~300 nm seed layer of flat WO_3 with a ~5 μm thick top layer of WO_3 nano-needles. At 1.23 V_{RHE}, this material showed incident photon-to-current efficiencies in the range ~35 – 45 % in the UV region (250 – 375 nm) and an overall solar predicted photocurrent of 1.24 $mA.cm^{-2}$ (~25 % of the theoretical maximum for WO_3). When coupled in tandem with a photovoltaic device containing a methyl ammonium lead iodide perovskite, a solar-to-hydrogen efficiency of *ca* 1 % for a complete unassisted water splitting device is predicted.

INTRODUCTION

It is widely acknowledged that the release of CO_2 from the combustion of fossil fuels is one of the primary causes of *Global Warming* – an effect that has resulted in increased average temperatures, melted polar ice and risen sea levels.[1,2] Sunlight has the potential to be our largest energy source, the amount reaching the Earth's surface each hour being almost twice the total energy consumed annually from fossil fuels, nuclear and all other renewable energy sources combined.[3] Consequently, solar cells are the fastest growing renewable technology. However, the biggest barrier to photovoltaics is the unpredictability of sunlight coupled with the mismatch between the times they work best and the times we need energy the most.[4] This is a major problem, as most electrical energy produced by photovoltaics must be used at the point of generation, as there is currently no integrated means of storing this energy.[5]

Photosynthesis is the perfect example of how plants use sunlight to produce fuel, which can be stored and used when required. This has resulted in many bio-inspired approaches – deemed *artificial photosynthesis*[6] – where arguably the most promising approach is the solar driven photolysis of water to produce hydrogen fuel from water using semiconductor photoelectrodes.[7] Numerous semiconductor materials have been examined for photoelectrochemical water splitting,[8] where metal oxides generally show several distinct advantages over other materials

(*e.g.* high resistance to photocorrosion in water, low toxicity, low synthetic cost and compatibility with up-scale). Some of the most promising metal oxide photoelectrodes include α-Fe_2O_3,[9] $BiVO_4$,[10] TiO_2[11] and WO_3.[12–19] WO_3 (E_{bg} ~2.7 eV, photocurrent onset ~0.5 V_{RHE})[18] is an promising candidate as it can absorb more of the solar spectrum than TiO_2 (3.0 eV, ~0.2 V_{RHE}),[11] begins to function at a lower onset potential than both $BiVO_4$ (2.4 eV, ~0.8 V_{RHE})[20,21] and α-Fe_2O_3 (2.1 eV, ~0.9 V_{RHE})[9,22] and is stable at low pH where H_2 evolution is often more efficient.[23] WO_3 photoanodes have been fabricated using numerous techniques, including sol-gel, hydrothermal, solvothermal, electrochemical, spray pyrolysis and physical sputtering methods,[17] and have reached current densities as high as 2.4 $mA.cm^{-2}$ at 1.23 V_{RHE}[14] under 1 sun illumination (~50 % of the theoretical maximum) showing a Faradaic efficiency of ~50 %. Similarly high current densities have been achieved in complete unassisted tandem cell devices composed of WO_3 photoanodes grown using a sol-gel method, coupled with a dye-sensitized solar cell.[24] Other studies have shown that the light absorption characteristics of WO_3 can be improved by intercalating Na or N_2 dopants[12,19] or by coupling with a semiconductor of narrower bandgap such as $BiVO_4$[25–27] or α-Fe_3O_4.[28]

Given the promise that WO_3 photoanodes have shown, there have been few studies detailing how complex WO_3 structures and coatings can be grown using an industrially applicable method. Many of the current methods to create complex or patterned coatings such as lithography are often laborious and time consuming, involving pattern, deposit and etch steps.[29] In this article, we demonstrate how complex nano-needle structures of WO_3 can be grown using an industrially applicable route, chemical vapor deposition (CVD). Importantly, CVD routes are highly scalable and can be applied to continuous fabrication or roll-to-roll processes, and is currently used heavily in industry to grow films and coatings on a large scale.[30] In the past, WO_3 photoanodes

have been grown using low-pressure CVD methods that are inherently less upscalable due to the requirement for low pressure.[31,32] They have also been grown using a flame CVD method at atmospheric pressure,[15] but required the use of a WO_3 seed layer that was first grown using a sol-gel method. In this article, we adapt an aerosol-assisted CVD method, previously used to grow WO_3-based gas sensing devices at atmospheric pressure.[33,34] The method was adapted so that combinations of flat or stacked nano-needle structures could be grown in two steps at different temperatures. These flat structures acted as a seed layer for growing more densely packed nano-needle structures. The effect of layer thickness for flat, nano-needle and combinations of the two structures were systematically studied. This allowed us to understand the relationship between a tailored nanostructure and material thickness for optimal light absorption and water splitting activity. The water splitting behavior of the best performing sample was characterized in depth, including its predicted performance when coupled in tandem with a photovoltaic cell containing a perovskite, methyl ammonium lead iodide, to form an unassisted water splitting device.

EXPERIMENTAL SECTION

Materials synthesis: WO_3 photoanodes were grown using an aerosol-assisted chemical vapor deposition (AACVD) process at atmospheric pressure (Figure S1a), using an adapted method to that previously reported by Blackman *et al*.[33] A picture of the AACVD apparatus is shown in Figure S1b. All materials were grown on FTO substrates (2.5 x 2.7 cm). The substrates were heated from underneath using a graphite heating block. The inlet to the reactor was equipped with a cooling water jacket. This was to prevent any prior decomposition of the precursor before reaching the reactor chamber. The stock precursor solution consisted of tungsten hexacarbonyl (0.6 g, 11.4 mM), dissolved in a mixture of acetone (100 ml) and methanol (50 ml). This stock

solution was sonicated for 10 minutes to dissolve the solid (VWR ultra-sonic cleaner, 30 W, 45 kHz) and stored in the dark. A set volume was used for each deposition, which was aerosolized using an ultrasonic humidifier (2 MHz, Liquifog – Johnson Matthey) and passed over the heated FTO substrate using an N_2 carrier gas (99.99 %, BOC) controlled by a mass flow controller (MFC, Brooks). For the growth of flat WO_3 materials, the reaction was conducted at 325 °C with a carrier gas flow rate of 500 sccm, transferring volumes of 1.0, 2.5, 5.0 or 10 ml. For the growth of nano-needle WO_3 structures, the reaction was conducted at 375 °C with a carrier gas flow rate of 300 sccm, transferring volumes of 2.5, 5.0, 10 or 20 ml. Three groups of samples were synthesized: (i) flat WO_3 materials, (ii) nano-needle WO_3 structures and (iii) a combination of flat WO_3 followed by nano-needle WO_3 structures grown on top. After the precursor solution had been completely transferred, the material was cooled to room temperature under a carrier gas flow of N_2. All deposited materials were post heat-treated at 500 °C in air for 12 hrs.

Physical Characterization: The surface morphology was investigated by scanning electron microscopy (SEM) on a JOEL-6301F field emission instrument. X-ray diffraction (XRD) patterns were measured with a modified Bruker-Axs D8 diffractometer with parallel beam optics equipped with a PSD LinxEye silicon strip detector. The instrument uses a Cu source for X-ray generation (V = 40 kV, I = 30 mA) with Cu $K_{\alpha 1}$ (λ = 1.54056 Å) and Cu $K_{\alpha 2}$ radiation (λ = 1.54439 Å) emitted with an intensity ratio of 2: 1. The incident beam was kept at 1° and the angular range of the patterns collected between $20 \leq 2\Theta° \leq 60$ with a step size of 0.05°. A Le Bail model was fit to each diffraction pattern using GSAS-EXPGUI software.[35] High-resolution transmission electron microscopy (HR-TEM) images were obtained using a high resolution TEM Jeol 2100 with a LaB_6 source operating at an acceleration voltage of 200 kV. Micrographs were recorded on a Gatan Orius Charge-coupled device (CCD). The films were scratched off the

quartz substrate using a scalpel, suspended in n-hexane, sonicated and then drop-casted onto a 400 Cu mesh lacy carbon grid (Agar Scientific Ltd.) for analysis. X-ray photoelectron spectroscopy (XPS) was carried out using a Thermo K-Alpha spectrometer with monochromated Al K_α radiation. Survey scans were collected over the 0 – 1400 eV binding energy range with 1 eV resolution and a pass energy of 200 eV. Higher resolution scans (0.1 eV) encompassing the principal peaks of C (1s), O (1s), F (1s), Si (2p), W (4f) and the valence band region (-5 to 15 eV) were also collected at a pass energy of 50 eV. Sub-surface layers were investigated by Ar-ion sputtering. Peaks were modeled using CasaXPS.[36] Peak positions were calibrated to adventitious carbon (284.5 eV) and peak areas were adjusted using the appropriate sensitivity factors to determine the population fraction of each state.[37] UV-visible transmittance and reflectance spectra were recorded over the 250 – 1100 nm range using a Helios double beam instrument equipped with an integrating sphere. Brunauer-Emmett-Teller (BET) surface area analysis (N_2 adsorption) was obtained using a TriStar II PLUS system (Micromeritics, Hertfordshire, UK) and processed using MicroActive™ software. Nanopowder was collected from CVD-produced films using a scalpel. 5 mg of the nanopowder was wrapped in tin foil and degassed overnight at 150 °C under flowing nitrogen gas. The relative pressure (P/P_0) was measured over the range 0.05 to 0.30 at 10 discrete points.

Photoelectrochemistry: All photoelectrochemical analyses were carried out in a home-made PEEK cell with quartz windows. The electrolyte was 0.5 M H_2SO_4 in Milli-Q-water (Millipore Corp., 18.2 MΩ.cm at 25 °C) (pH = 0.56). A three-electrode configuration was used, with a Pt mesh counter electrode, a Ag/AgCl/saturated-KCl reference electrode (0.197 V_{NHE} at 25 °C; Metrohm) and the WO_3 photoanode as the working electrode.

On measuring current-voltage curves, a 365 nm LED light source was used (LZ1-10U600, LedEngin. Inc.) to photo-excite the materials. The light intensity was measured using an optical power meter (PM 100, Thorlabs) coupled with a power sensor (S120UV, Thorlabs). An Autolab potentiostat (PGSTAT12 with an FRA2 module) was used to apply voltage and measure currents. The applied voltages are reported *vs* the reversible hydrogen electrode (V_{RHE}), converted using the Nernst equation:

$$V_{RHE} = V_{Ag/AgCl} + 0.0591 \times pH + V^{o}_{Ag/AgCl} \quad \text{(Equation 1)}$$

The incident photon to current efficiency (IPCE) was measured using an ozone-free xenon lamp (75 W, Hamamatsu) coupled with a monochromator (OBB-2001, Photon Technology International). The IPCE was calculated using the following equation:

$$IPCE\ (\%) = \frac{I_{ph} \times 1239.8}{P_{mono} \times \lambda} \times 100 \quad \text{(Equation 2)}$$

where I_{ph} (mA.cm^{-2}) is the photocurrent, 1239.8 (eV.nm) is a multiplication of Planck's constant with the speed of light, P_{mono} (mW.cm^{-2}) is the power and λ (nm) is the wavelength of the monochromated light.

The solar water splitting activity of the WO_3 photoanodes were predicted from IPCE measurements. This solar predicted photocurrent (SPP) was determined by multiplying the IPCE with the AM1.5 solar spectrum, and then converting this into a current:

$$SPP\ (mA.cm^{-2}) = \int_{3000\ nm}^{280\ nm} IPCE \times AM1.5\ (photon.cm^{-2}) \times 1000/\ 1C$$

(Equation 3)

where $1C$ is 6.241 x 10^{18} electrons per second. The solar-to-hydrogen efficiency (η) could be calculated from this solar predicted photocurrent:

$$\eta\ (\%) = \frac{SPP\ (mA.cm^{-2}) \times (1.23V - V_{app})}{P_{in}\ (mW.cm^{-2})} \times 100 \qquad \text{(Equation 4)}$$

where V_{app} is the voltage applied when measuring the SPP and P_{in} is the power of AM1.5 solar light (100 mW.cm^{-2}).

Faradaic efficiency measurements were carried out in a gas tight, three electrode electrochemical cell. The sample was held at 1.23 V_{RHE} in 0.5 M H_2SO_4 (pH = 0.56) in the presence of a UV light source (365 nm LED, ~30 mW.cm^{-2}). The oxygen evolution was analyzed with a gas-phase Clark-type oxygen electrode (Unisense Ox-N needle microsensor). At the end of the experiment the cell was calibrated by adding known amounts of air. The Faradaic efficiency (FE) was estimated using the following equation:

$$FE\ (\%) = \frac{real\ moles\ of\ O_2}{theoretical\ moles\ of\ O_2} \times\ 100 \qquad \text{(Equation 5)}$$

where real moles of O_2 were quantified using a Clark electrode in the gas phase and the theoretical moles of O_2 was the amount of oxygen that the system could produce, assuming a 100% Faradaic conversion efficiency. The latter was estimated from photocurrent measurements, which can be converted into mol of O_2 taking into account the Faraday constant (96485 C / mole of electrons) and the requirement of 4 electrons to produce 1 mol of oxygen.

RESULTS AND DISCUSSION

WO_3 photoanodes were grown using an aerosol-assisted chemical vapor deposition (AACVD) method. Those grown at 325 °C were flat, smooth and well adhered to the FTO substrate. Those grown at 375 °C appeared hazy and were less well adhered to the FTO substrate (they did not

pass the Scotch Tape test). Upon inspection by scanning electron microscopy (SEM), materials grown at 325 °C were flat dense structures, whereas those grown at 375 °C were composed of nano-needle structures primarily aligned perpendicular to the substrate. Both sets of as-deposited materials were initially blue in color, and turned pale yellow after their heat treatment at 500 °C in air.

In order to find a sample of optimum performance, a series of WO_3 photoanodes were grown in a systematic manner – fixing the volume of precursor transferred in each deposition. Three types of structure were grown: (i) flat, (ii) nano-needle or (iii) flat with nano-needles grown on top. For the purpose of brevity, we will refer to each sample for the remainder of this manuscript using a simple code system. First, the type of deposition is stated using a letter, where "F" represents flat structures and "NN" represents nano-needle structures. The letter is then followed by the approximate thickness as measured by side-on SEM imaging. For dual layers, the two types of deposition are comma separated. For example, a WO_3 photoanode grown with 5 ml of precursor solution at 325 °C and then subsequently 10 ml of precursor solution at 375 °C is called: F ~500 nm, NN ~4.6 µm. A photograph of the WO_3 photoanodes studied herein is shown in Figure 1.

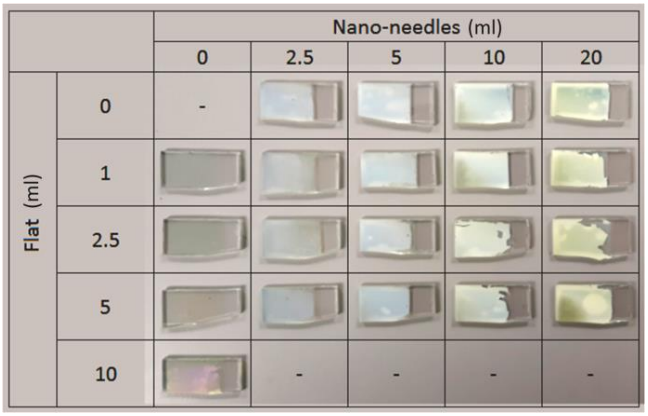

Figure 1. A photograph of the WO_3 photoanodes studied herein, positioned in a table that shows the precursor volumes transferred during their synthesis to grow flat WO_3 and/or nano-needle structured WO_3 on top. Flat WO_3 was grown at 325 °C and nano-needle structured WO_3 was grown at 375 °C.

Surface topographies were investigated by SEM. Micrographs for select samples are shown in Figure 2. One example is shown for a flat structure, F ~800 nm, which was composed of rounded particles approximately 100 nm in diameter. Film thickness was measured by looking at the materials side-on, which increased from ~200 to ~800 nm for flat samples (Table S1). The topography for one example of a nano-needle structure (with no flat layer grown beneath), NN ~4.2 μm, is also shown in Figure 2. Nano-needles were around 4 μm long and were roughly 100 nm in diameter. In general, these needles were aligned vertically from the substrate. The effect of increasing precursor volume is also shown for a series of flat samples (F ~300 nm) with nano-needles grown on top (N ~2.3, 4.6 and 6.2 μm). As the volume of precursor transfer increased, both the length and width of the nano-needles also increased. At higher deposition volumes, the tips of the nano-needles began to merge. An example side on SEM image for sample F ~300 nm, NN ~4.6 μm is shown in Figure S2. Needles were primarily aligned perpendicular to the substrate, and stacked on top of each other to some degree. It is worthy of note that the complex nano-needle structures observed herein are not so readily formed in other photoelectrode materials, and often require multiple steps or expensive patterning methods such as lithography to achieve similar nanostructure.[29]

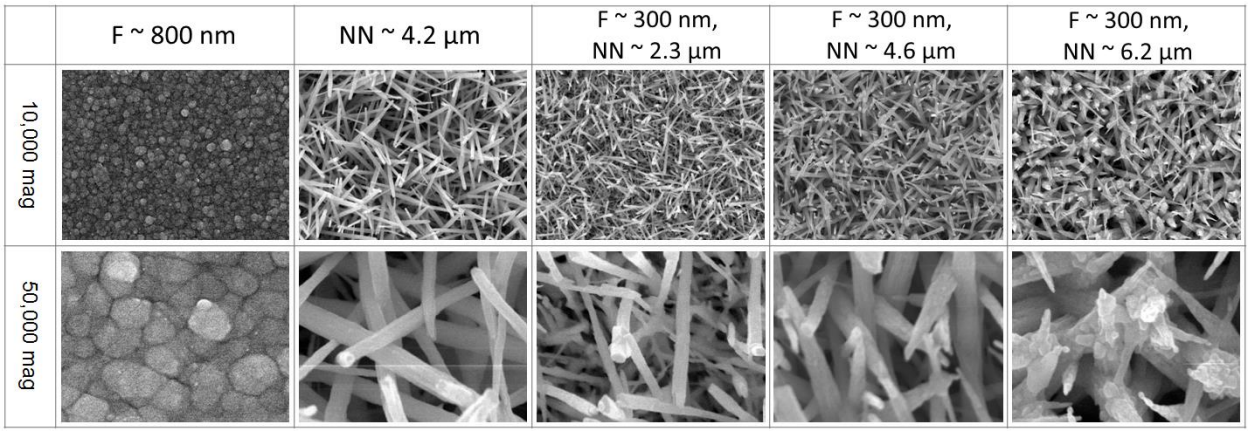

Figure 2. Top down SEM images of select WO_3 photoanodes at 10,000 and 50,000 magnification. The width of images taken at 10,000 and 50,000 magnifications are 7.0 and 1.4 µm respectively.

X-ray diffraction (Figure 3) showed that all WO_3 photoanodes produced herein were phase pure and adopted the monoclinic γ-WO_3 structure ($P2_1/n$, a = 7.30084(7), b = 7.53889(7), c = 7.68962(7) Å, β = 90.892(1)°).[38] In thinner films, peaks corresponding to the FTO substrate were also observed. A Le Bail model was fit to each diffraction pattern. All WO_3 photoanodes produced herein possessed unit cells marginally larger than a powder standard (~0.4 to 1.0 % expansion), albeit with no clear correlation (Table S1). However, there were other discernible relationships. For instance, average crystal size partly increased with the volume of precursor transferred. More striking were the changes in preferred growth, where the tendency to grow in the (002) direction also increased with precursor volume transferred in flat dense structures (Figure S3). However, for nano-needle structures, the tendency to grow in the (002) direction was consistently high.

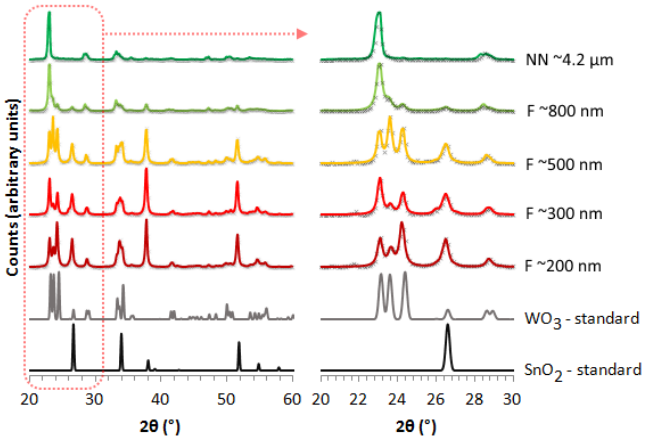

Figure 3. XRD patterns of select samples (cross-hairs) plot alongside their Le Bail model (solid colored lines). The right graph shows a close-up of the region where the largest changes in preferred growth were observed.

The physical properties of the nano-needle structures were further investigated using high-resolution transmission electron microscopy (HR-TEM). The average nano-needle length increased with precursor volume transferred (Figure S4). For the series of nano-needles grown on F ~300 nm, average nano-needle length increased from ~0.7 to ~2.5 µm. These lengths were substantially shorter than the film thicknesses observed by side-on SEM imaging (Table S1). This was because needles grew on top of one another, to some extent, as they grew from the substrate beneath. The needles were highly ordered and showed a strong tendency to grow in the (002) direction (Figure 4). The surface area of a nano-needle sample (F ~300 nm, NN ~4.6 µm) was measured using BET analysis (~20 ± 10 $m^2.g^{-1}$), which corresponded to a surface area of around 100 cm^2 per projected area of 1 cm^2.

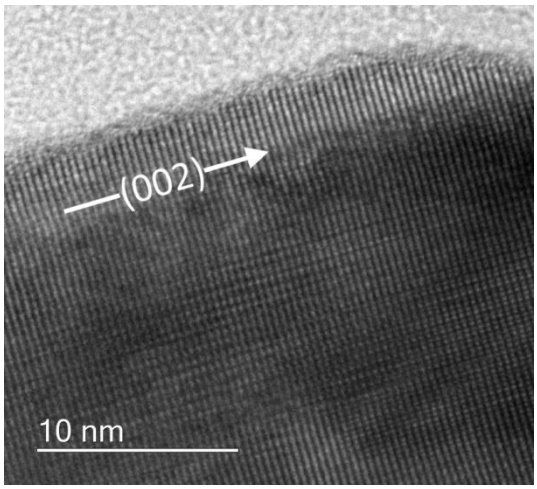

Figure 4. HR-TEM image of the edge of a nano-needle (F ~300 nm, NN ~4.6 μm). The spacing between the highly ordered rows of atoms correlates to the d-spacing found in the (002) plane of monoclinic WO_3 (~3.86 Å).

X-ray photoelectron spectroscopy (XPS) was used to study the oxidation states and impurity levels for a number of WO_3 samples. Analysis of the W 4f environment showed no measurable presence of W^{5+} states, and solely the W^{6+} environment, with binding energies similar to reference values (Figure S5a).[39] Although not discernible in the W 4f region, W^{5+} states were observed at low binding energies (at ~ 0 eV), albeit in low concentration (W^{5+}: W^{6+} ~1: 2000). Analysis of this W 5d cross-section revealed a W^{5+} concentration of around 1 x 10^{19} cm^{-3}. No impurities were observed, with the exception of carbon, which may have been a result of the incomplete decomposition of the $W(CO)_6$ precursor. Samples were sputtered to probe carbon impurity levels in the bulk (Figure S5b). Nano-needle structures showed little or no presence of carbon in the bulk after 60 s of sputtering. However, flat structures showed carbon impurities deeper into the bulk. In the thinnest sample (F ~200 nm thick), the carbon impurity level did not reach zero (with respect to surface carbon levels) after 1200 s of sputtering. As film thickness increased, a zero carbon impurity level was reached more quickly, where the thickest flat sample

(F ~800 nm thick) showed no bulk carbon impurities after 300 s of sputtering. Valence band energy regions were also investigated (Figure S5c). The edge of each valence region was extrapolated to the energy axis to determine the energy of the valence band maximum. These energies are shown on a band energy diagram, where the energy level is relative to the Fermi level of each material, set at zero (Figure S5d). In general, nano-needles possessed less positive valence band energies. Also, in flat materials, the valence band energy was less positive in thicker films. Physical characterizations showed that there were only two significant differences between thin flat films and thicker flat films/ nano-needle structures: (i) the degree of preferred growth in the (002) crystal plane and (ii) the carbon impurity level. The observed differences in valence band energy may be associated with either physical property.

The optical properties of the WO_3 photoanodes were assessed using UV-visible spectroscopy (Figure 5a). Flat WO_3 structures showed a high degree of transmission in the visible and near infrared. Nano-needle structures became increasingly scattering in this region with increasing nano-needle length. Moreover, as the needles increased in length, an increasingly red-shifted band edge was observed. This increased from ~320 nm in F ~200 nm (no nano-needles present) to ~420 nm in F ~300 nm, NN ~6.2 μm. Optical bandgaps were determined from Tauc plots[40] (Figure S6). A wide range of optical bandgaps were observed, ranging from ~3.0 eV in sample F ~200 nm to ~2.6 eV in sample F ~300 nm, NN ~6.2 μm (Figure 5b). As all of the WO_3 photoelectrodes adopted the same crystal structure (monoclinic γ-WO_3) and showed similar lattice and crystallite sizes, the observed differences in bandgap energy may be due to changes in carbon impurity levels, preferential crystal growth or nano-needle length.

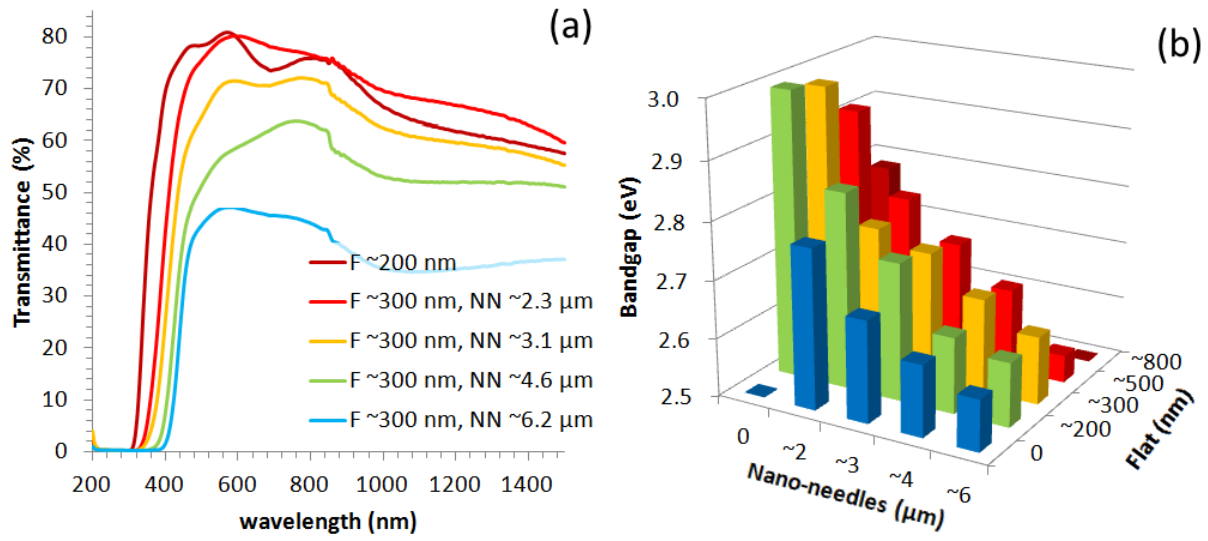

Figure 5. (a) UV-visible spectroscopy showing the transmission of light for select WO_3 samples and (b) a 3D bar chart showing the optical bandgap of all WO_3 samples made herein – derived from Tauc plots.

The water oxidation function of the WO_3 photoanodes was assessed photoelectrochemically. Current-voltage curves were measured by sweeping the voltage from 0.45 V_{RHE} to 2.45 V_{RHE} in the dark and under the action of light (Figure 6). In the dark, electrocatalytic water oxidation was observed from ~2.0 V_{RHE} and above in both flat and nano-needle structures. This was due to the thermodynamic requirement for water oxidation to be surpassed (1.23 V_{RHE}) plus the additional over-potential, which is typically quite high for this kinetically challenging process (*ca.* 0.4 V and above).[41] In flat dense structures, photocatalytic currents decreased when film thickness increased (Figure 6a). In nano-needle structures, comparatively higher photocatalytic currents were observed (Figure 6b), typically five times higher than what was observed in flat materials. Although the onset potentials for photocatalytic oxidation were similar in both flat and nano-needle structures (~0.5 V_{RHE}), the photocurrent increased more steeply in nano-needles

structures; reaching a plateau from almost 0.8 V_{RHE}. From ~2.2 V_{RHE}, electrocatalytic oxidation dominated and photocatalysis was not observed.

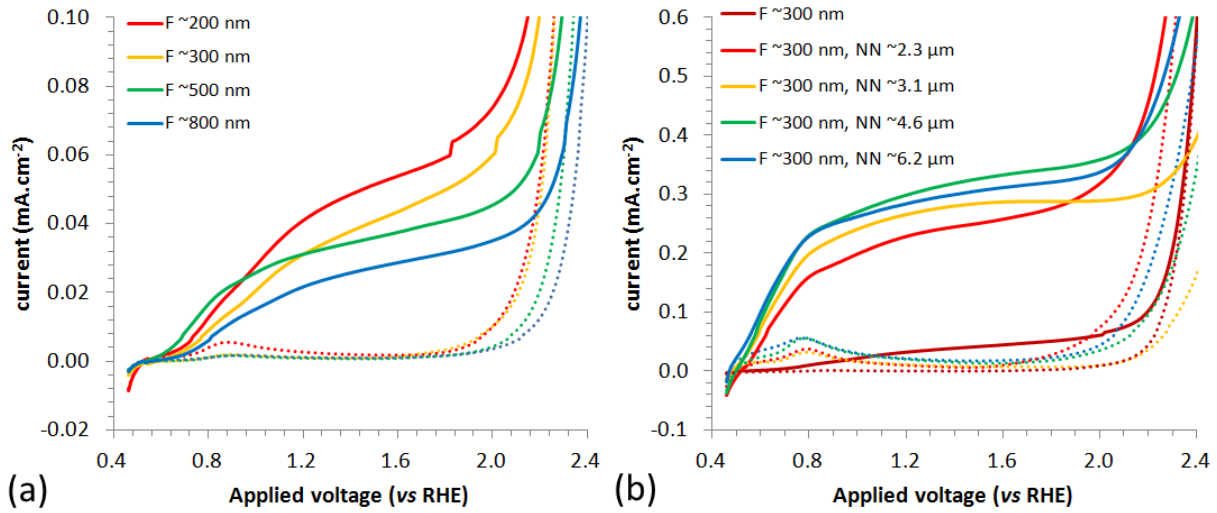

Figure 6. Current-voltage curves of (a) a series of flat WO_3 photoanodes and (b) a series of nano-needle photoanodes with constant flat layer thickness beneath. Samples were measured in the dark (dashed lines) and under the action of light (solid lines; 365 nm LED – 4.2 $mW.cm^{-2}$). The voltage was swept from cathodic to anodic potentials (0.45 – 2.45 V_{RHE}) at a rate of 50 $mV.s^{-1}$ in 0.5 M H_2SO_4 (pH = 0.56). Samples were irradiated at the semiconductor-electrolyte interface.

The incident photon-to-current efficiency (IPCE) was measured at a range of wavelengths for each sample, holding the photoanode at 1.23 V_{RHE} (the thermodynamic potential for water oxidation). Samples were irradiated from either the front (semiconductor-electrolyte interface) or back (electrode-electrolyte interface). When considering arrangements within a tandem cell device, it is particularly useful to examine the photocatalytic performance of a photoelectrode under both front and back irradiation (Figure S7). For flat materials, the quantum efficiency was in the range 20 to 30 % in the UVC (range 250 – 300 nm) upon front irradiation, which steadily declined to 0 % in the near visible (450 nm, Figure S8a). When irradiating from the back, the

quantum efficiency was substantially lower in the UVC region (Figure S8b). This was due to the unfavorable absorption of light by the FTO electrode (E_{bg} ~3.6 eV), which shielded the WO_3 layer from UVC irradiation. However, comparing results from front and back irradiation, similar efficiencies were observed from 350 nm and above. In flat WO_3 materials, IPCEs decreased as film thickness increased.

In nano-needle structures, quantum efficiencies in the UVC region were similar to flat materials, in the range ~25 to 30 % (Figure 7a). In stark contrast to flat materials, the quantum efficiency increased on movement into the UVA region (range 325 – 375 nm), with efficiencies in the range ~30 to 45 %. In general, thicker nano-needle structures possessed higher levels of visible light activity. The quantum efficiency in the UVC was substantially reduced when irradiating from the back, due to unfavorable light absorption by the FTO substrate (Figure 7b).

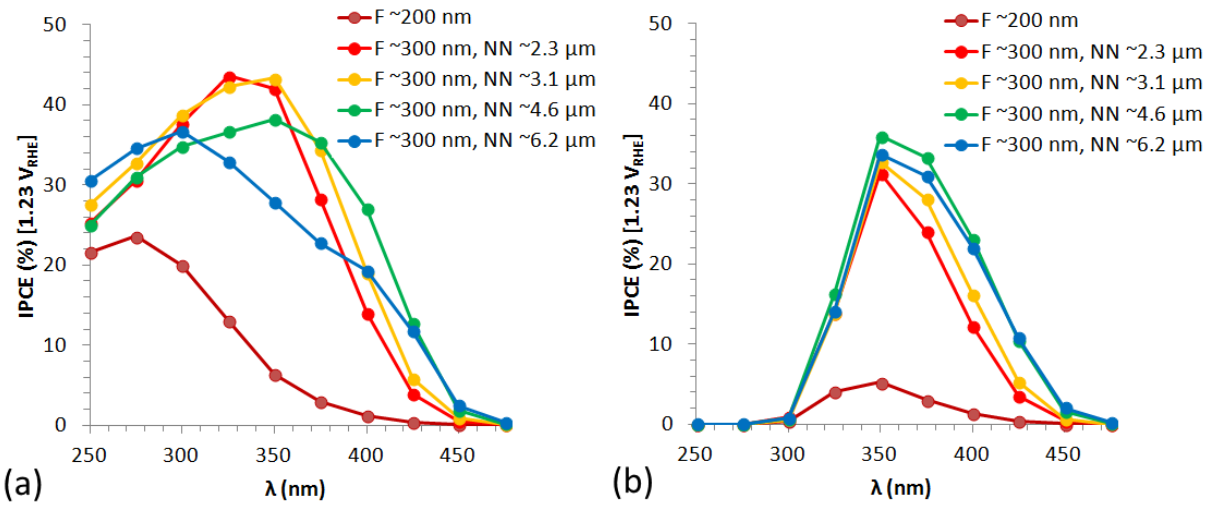

Figure 7. Incident photon-to-current efficiencies (IPCE) for select WO_3 photoanodes. Samples were measured at 1.23 V_{RHE} in 0.5 M H_2SO_4 (pH = 0.56) under (a) front [semiconductor-electrolyte interface] and (b) back [electrode-electrolyte interface] illumination. Each wavelength was selected using a monochromator using a Xe light source (~10 $mW.cm^{-2}$ over the range of wavelengths studied).

To predict which WO_3 photoanode would be best suited for solar water splitting applications, we determined a solar predicted photocurrent (SPP) for the 20 unique samples studied herein. This was determined by multiplying the IPCE with the AM1.5 solar spectrum using Equation 3, shown graphically in Figure 8 for sample F ~300 nm, NN ~4.6 µm.

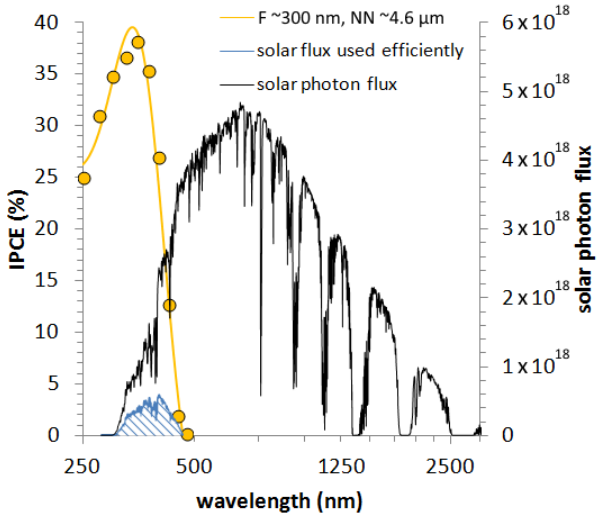

Figure 8. The theoretical portion of solar light that would be converted into photocurrent by sample F ~300 nm, NN ~4.6 µm when held at 1.23 V_{RHE}.

As solar light contains few UVC photons, the relatively high quantum efficiency seen in this region is of little benefit for solar applications. However, materials that possessed higher efficiencies in the UVA and near visible would be of greater benefit. Therefore, the nano-needle structures, which showed higher IPCEs in the near-visible, showed higher solar predicted photocurrents compared with flat structures (Figure 9).

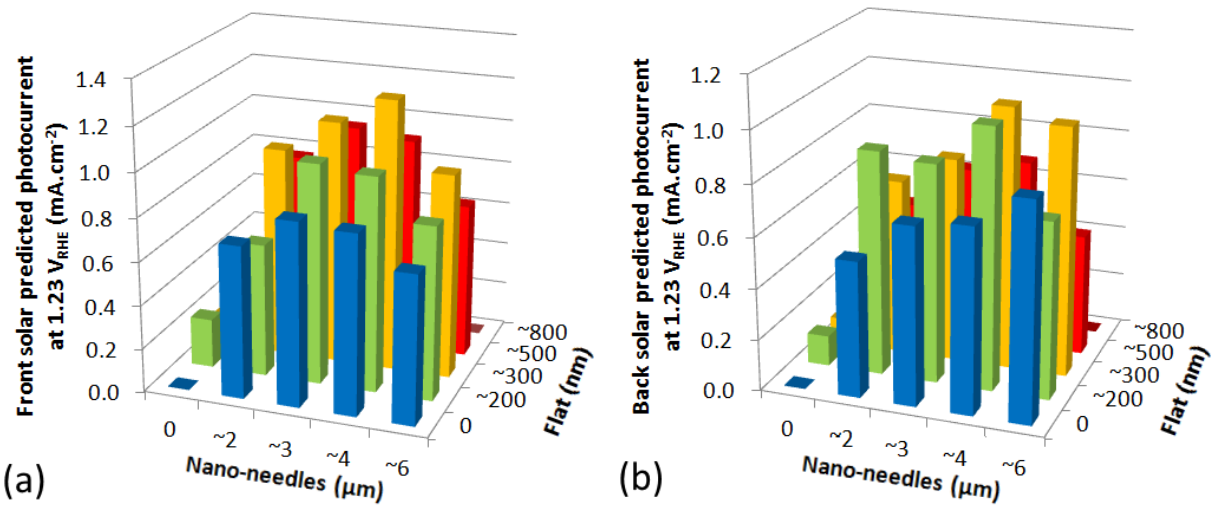

Figure 9. Solar predicted photocurrents for all WO_3 photoanodes for both (a) front and (b) back illumination. These photocurrents were predicted from IPCE measurements conducted at 1.23 V_{RHE} in 0.5 M H_2SO_4 (pH = 0.56) using Equation 3.

In general, SPPs showed that WO_3 nano-needles were *ca* 3 to 5 times more active than their flat counterparts. However, materials composed of both a flat "seed" layer with nano-needles grown on top were notably more active than needles alone. The authors attribute this to the greater density of nano-needles formed when a seed layer was present (Figure 2). The SPPs were calculated for both cases of front and back irradiation. Generally, back irradiation resulted in slightly lower SPPs (because of unfavorable light absorption by the FTO layer). Looking at the SPPs for front irradiation (Figure 9a), a clear trend to the best performing sample was observed; F ~300 nm, NN ~4.6 µm. Looking at the SPPs for back irradiation (Figure 9b), a trend was less clear. What could be said was that nano-needle structures with flat "seed" layers between ~200 – 300 nm in thickness (F ~200 – 300 nm) were the most active. Although there was no clear trend in the case of back irradiation, the best performing sample was again sample F ~300 nm, NN ~4.6 µm.

The solar predicted photocurrents observed herein (0.06 – 1.24 mA.cm^{-2}) are now compared with the literature (Table 1). Lee *et al.* hydrothermally grew monoclinic WO_3 nanocrystals, and doctor-bladed them to form a mesoporous photoelectrode.[42] Under AM1.5 solar simulated light, they observed photocurrents of ~0.6 mA.cm^{-2} at ~1.23 V_{RHE} and reported an IPCE of ~25 % at 340 nm. Grimes *et al.* solvothermally grew WO_3 nanowire structures, which showed IPCEs of ~60 % at 400 nm and photocurrents of ~1.4 mA.cm^{-2} when held at 1.23 V_{RHE} and exposed to AM1.5 solar simulated light.[43] Fàbrega *et al.* grew WO_3 nano-needle structures using a pulsed laser deposition process, which showed photocurrents of 2.4 mA.cm^{-2} at 1.23 V_{RHE} under AM1.5 solar simulated light.[18] WO_3 photoanodes have also previously been grown using CVD processes. Sunkara *et al.* grew WO_3 nano-needle structures at reduced pressure (~100 Pa) using a hot-wire technique.[31] These photoanodes showed photocurrents of ~1.0 mA.cm^{-2} at 1.23 V_{RHE} under AM1.5 solar simulated light. Rao *et al.* also grew WO_3 nano-needle structures by CVD, this time at atmospheric pressure.[15] In their case, a seed layer grown using wet-chemical methods was required to promote dense and uniform growth of nano-needles. Under AM1.5 solar simulated light these photoanodes reached photocurrents of ~1.6 mA.cm^{-2} at ~1.3 V *vs* a Pt counter electrode using a 2 electrode configuration.

Table 1. Summary of the synthesis, microstructure and photocatalytic water oxidation activity for various WO_3 photoanodes reported in the literature.

Synthesis[a]	Microstructure	Photocatalytic activity		Reference
		Photocurrent[b]	IPCE	
Hydrothermal	Mesoporous film of inter-connected WO_3 nanospheres (each ~50 nm in diameter, forming a film ~9 μm thick)	~0.6 mA.cm^{-2}	~25 %, 340 nm	Lee *et al* [42]

Spin-coating + Solvothermal	Array of vertically aligned nanoflakes (~20 – 30 nm thick and ~5.6 µm wide)	~1.4 mA.cm^{-2}	~60 %, 400 nm	Grimes *et al.*[43]
Pulsed laser deposition (~13 Pa)	Array of closely-packed, vertically aligned nano-needles (~17.6 µm long)	~2.4 mA.cm^{-2}	~50 %, 410 nm	Fàbrega *et al.*[18]
CVD (~100 Pa)	Array of vertically aligned nano-needles (~40 – 70 nm in diameter and ~2 – 3 µm long)	~1.0 mA.cm^{-2}	~35 %, 425 nm	Sunkara *et al.*[31]
Spin-coating + CVD	Array of vertically aligned hollow nano-needles (~15 µm thick)	~1.6 mA.cm^{-2} [c]	-	Rao *et al.*[15]
CVD	Flat WO_3 films (~200 – 800 nm thick)	~0.1 – 0.2 mA.cm^{-2} [d]	~2 %, 400 nm	herein
CVD	Array of vertically aligned nano-needles (~100 nm in diameter and ~2 – 6 µm long)	~0.6 – 1.24 mA.cm^{-2} [d]	~27 %, 400 nm	herein

[a] synthesis conducted at atmospheric pressure unless specified; [b] photocurrent at 1 sun irradiance (AM1.5 solar simulated light, 100 mW.cm-2) and a applied potential of 1.23VRHE; [c] photocurrent achieved at ~1.3 V vs a Pt counter electrode in a 2 electrode configuration; [d] solar predicted photocurrents (see Equation 3).

Photon penetration depths (Figure 10) were determined from a flat sample of known thickness (F ~300 nm thick). Absorption coefficients were calculated from transmission data:

$$\alpha\ (cm^{-1}) = -\frac{\ln T}{l\ (cm)} \qquad \text{(Equation 6a)}$$

where T is the fraction of transmitted light and l is material thickness. The penetration depth was then solved analytically, where for a given fraction of light absorbed, δ, the exponent y was determined:

$$\delta = 1 - \left(\frac{1}{e^{y}}\right) \qquad \text{(Equation 6b)}$$

where y/α is the photon penetration depth. Using the photon penetration depth, differences in light conversion behaviour between materials of nano-needle and flat structure were rationalized. This was done keeping in mind the respective electron (~7 μm)[44] and hole diffusion lengths (~150 nm)[45] of WO_3.

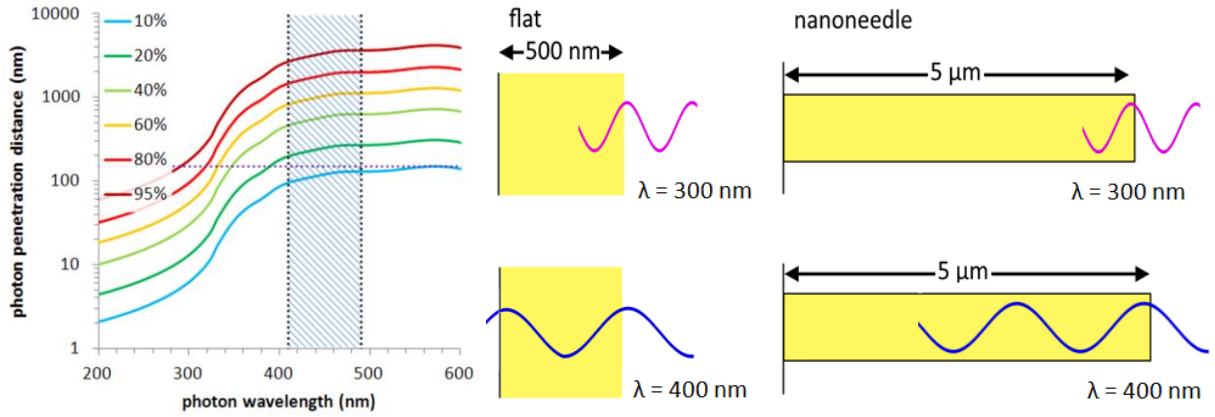

Figure 10. (left) Photon penetration depth for a range of light fractions absorbed. The purple dashed horizontal line represents the hole diffusion length in WO_3 (~150 nm). The blue dashed area represents the range of bandgaps found in the WO_3 photoanodes. (right) Visual examples showing where light of different wavelengths are absorbed in WO_3 materials of flat or needle structure.

Considering the case of front irradiation (semiconductor-electrolyte interface) in a flat material, 95 % of UV light (range 250 – 300 nm) would be absorbed within the first 150 nm (Figure 10). As such, holes would be capable of diffusing back to the semiconductor-electrolyte interface and taking part in photocatalytic reactions. However, in the case of near-visible light (400 nm), less than 20 % of light would be absorbed within the first 150 nm, meaning a large portion of holes would be incapable of diffusing back to the semiconductor-electrolyte interface. This was reflected in the IPCE spectra of flat materials in that efficiencies were higher in the UVC region (range 250 – 300 nm, ~20 %) compared with the near-visible region (400 nm, ~2

%). Now if we consider the case of front irradiation of a nano-needle structured material, there is no requirement for holes to diffuse back to the material surface, as the needles are exposed to water on all fronts. As needles were ~100 nm wide, holes would be able to diffuse to the semiconductor-electrolyte interface wherever generated inside the needle. In addition to this, thicker nano-needle structures (> 4 μm) were sufficiently long to facilitate complete light absorption in the near-visible range. This was reflected in the IPCE spectra of nano-needle structures, where efficiencies were consistently high across the UVC and near-visible regions (range 250 - 400 nm, ~20 – 40 %). However, as the thickness of the nano-needle structures grown herein increased from ~4 to ~6 μm, a small decrease in activity was observed, which coincided with an approach to the electron diffusion length limit.

The stability of the best performing sample, F ~300 nm, NN ~4.6 μm, was evaluated over a period of 4 hours (Figure S9). Simulating conditions of device operation, the material was held at a positive potential for several hours under the action of chopped UV light. For comparison, a flat structure was also examined, F ~500 nm. Photocurrents were superior in the nano-needle structured material, but were initially less stable, dropping by ~20 % in the first 30 minutes. After 210 minutes, the photocurrent stabilized, but was ~40 % lower than the initial value. In the flat structured material, the photocurrent marginally increased before stabilizing, and showed no loss in performance over the testing period. The loss in performance in the nano-needle structures produced herein was attributed to the poor adherence of needles to the FTO substrate, which flaked off during testing. This was more prominent in photoelectrodes with thicker nano-needle stacks (NN > 4μm) and occurred less so in thinner nano-needle structures (NN < 3 μm). Recent studies have shown that the stability of nanostructured WO_3 photoanodes can be increased when co-catalysts such as nickel borate[46] and iron oxy-hydroxide[47] are grown at the

surface; where these co-catalysts also improve the Faradaic efficiency of water oxidation. Choi *et. al.* studied a range of electrolytes and found that the use of acetate based electrolytes improved photostability substantially compared with phosphate, perchlorate and chloride based electrolytes.[48] The Faradaic efficiency of the best performing sample, F ~300 nm, NN ~4.6 μm, was also measured, yielding a Faradaic efficiency of ~64 % (Figure S10). Deviations from Faradaic unity are common in WO_3 photoelectrodes, and have been attributed to the material's deeply oxidizing valence band.[48] Previous studies of WO_3 photoelectrodes in sulfate solutions have shown that water oxidation to di-oxygen competes with sulfate oxidation to persulphate[50] and incomplete water oxidation to form peroxo species[51] (which accumulate on the material surface and cause a gradual decay in the , also observed herein). A comprehensive study of the Faradaic efficiencies of water oxidation for WO_3 photoelectrodes was recently conducted by Choi *et al*.[48] Their studies showed that water oxidation was inhibited in highly acidic solutions, where a Faradaic efficiency of 35 % was recorded in pH = 1. In these studies, the Faradaic efficiency of water oxidation was almost double that observed by Choi *et al.* for a similarly acidic pH. We believe that this enhancement in selectivity may be due to the preferential crystal growth of nano-needle structures and is currently the subject of an ongoing study.

The IPCE of the best performing sample, F ~300 nm, NN ~4.6 μm, was measured at a range of applied potentials. This allowed us to create a 3D contour map of efficiency *vs* wavelength and applied potential (Figure 11). IPCE decreased almost linearly with applied potential, and followed a similar trend to its current-voltage curve (Figure 6b). For a given applied potential, the measured IPCE was used to calculate the solar predicted photocurrent (SPP), which in turn was used to determine solar-to-hydrogen efficiencies using Equation 4. For a voltage-assisted

water splitting device, solar-to-hydrogen efficiencies peaked at 0.9 V_{RHE} for both front (η = 0.25 %) and back (η = 0.21 %) irradiation (Figure S11).

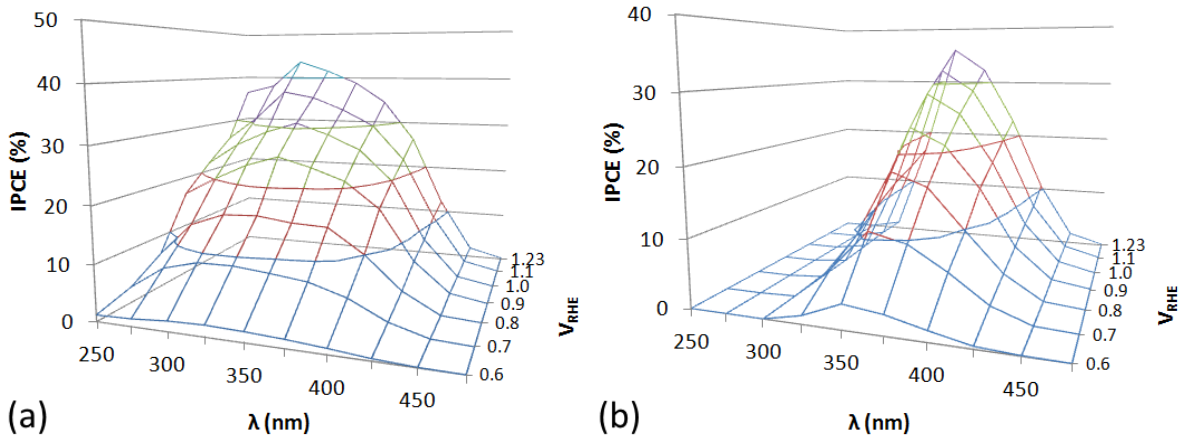

Figure 11. The change in incident photon-to-current efficiency (IPCE) at various applied potentials in 0.5 M H_2SO_4 (pH = 0.56) for the best performing sample, F ~300 nm, NN ~4.6 µm. The sample was measured under (a) front [semiconductor-electrolyte interface] and (b) back [electrode-electrolyte interface] illumination. Each wavelength was selected using a monochromator using a Xe light source (~10 $mW.cm^{-2}$ over the range of wavelengths studied).

The ability of the best performing WO_3 photoanode produced herein to work in tandem with a solar cell was also assessed. A methyl ammonium lead iodide perovskite solar cell was chosen, as it can provide the high voltage required for WO_3 photoanodes to operate (V_{oc} = 0.96 V, J_{sc} = 16.1 $mA.cm^{-2}$, FF = 0.45, efficiency = 7 %). The architecture and synthetic details of how the solar cell was made is described in a previous publication.[52] As the WO_3 photoanode possesses the wider bandgap, light must be passed through the back of this material first (tandem cell arrangement shown in Figure S7b). Under operating conditions, the solar cell provided 0.85 V of potential. As the solar cell provided 0.85 V of potential, current-matching between the WO_3 photoanode and a Pt electrocatalyst showed that the photoanode would operate at 0.8 V_{RHE}

(Figure S12b). The IPCE of the WO_3 photoanode at 0.8 V_{RHE} under back irradiation was used to determine the solar predicted photocurrent (~0.6 $mA.cm^{-2}$, Figure 12). Similarly, the IPCE of the solar cell, measured through a WO_3 filter, was used to determine the solar predicted current (~3.5 $mA.cm^{-2}$). The tandem cell was limited by the performance of the WO_3 photoanode, as it generated a lower photocurrent than the solar cell. We predict the overall solar-to-hydrogen efficiency of the tandem cell to be ~0.75 %. Similar work conducted by Kamat *et al.* showed that a tandem cell consisting of a $BiVO_4$ photoanode coupled with a perovskite solar cell could achieve solar-to-hydrogen efficiencies of ~2.5 %.[53] We attribute their higher performance to the increased solar light absorption of $BiVO_4$ (E_{bg} ~2.4 eV) compared with WO_3 (E_{bg} ~2.7 eV). Similarly, Sivula *et al.* showed that tandem cells consisting of either an α-Fe_2O_3 or WO_3 photoanode paired with a dye-sensitized solar cell can reach solar-to-hydrogen efficiencies of ~1.2 % and ~3.1 % respectively.[24] We attribute the higher performance of Sivula *et al.*'s WO_3-based tandem cell to the higher operating voltage of his solar cell (~1.0 V) and the higher light conversion efficiency of his WO_3 photoanodes, grown using a sol-gel process.

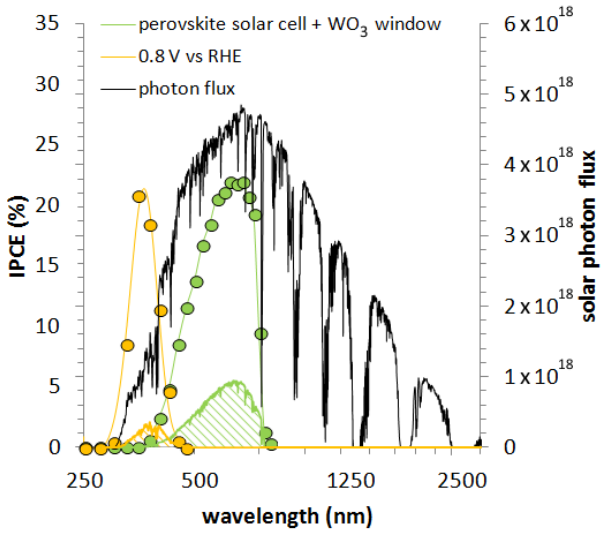

Figure 12. The theoretical solar performance of a tandem cell device consisting of a WO_3 photoanode (sample F ~300 nm, NN ~4.6 µm, first light absorber) and a perovskite solar cell

(second light absorber). As the solar cell provided 0.85 V of potential, current-matching between the WO_3 photoanode and a Pt electrocatalyst showed that the photoanode would operate at 0.8 V_{RHE}.

CONCLUSIONS

In this article, a route to produce WO_3 photoelectrodes is developed using chemical vapor deposition at atmospheric pressure – a low-cost technique use widely for the mass-production of nanoscale coatings. We believe that this is the first time in which WO_3 photoanodes have been entirely fabricated using chemical vapor deposition processes at atmospheric pressure. The chosen synthesis method offers a direct, inexpensive and scalable route with promising potential for future scale-up. Two growth conditions were investigated, one in which flat and dense WO_3 structures were grown at 325 °C and the other in which stacked nano-needles were formed at 375 °C. These two growth conditions, and their combinations, were systematically studied in order to determine the conditions for optimal water splitting performance. Photoelectrodes that showed the highest efficiencies were composed of a ~300 nm seed layer of flat WO_3 with a ~5 μm thick top layer of WO_3 nano-needles. When held at 1.23 V_{RHE}, this material showed incident photon-to-current efficiencies of ~40 % in the UV region (from 250 – 375 nm) and a solar predicted photocurrent of 1.24 $mA.cm^{-2}$ (~25 % of the theoretical maximum). When coupled in tandem with a photovoltaic device containing a methyl ammonium lead iodide perovskite absorber, we predict a solar-to-hydrogen efficiency of roughly 1 % for a complete unassisted water splitting device.

AUTHOR INFORMATION

Corresponding Author

*corresponding author; e-mail: a.kafizas@imperial.ac.uk

Author Contributions

The manuscript was written through contributions of all authors. All authors have given approval to the final version of the manuscript.

ACKNOWLEDGMENT

AK would like to thank Imperial College London for a Junior Research Fellowship. LF thanks the EU for a Marie Curie fellowship (658270). YL thanks the China Scholarship Council (CSC File No. 201406370157) for funding, and the UCL Dean's prize for the joint PhD scholarship. CS-V thanks the European Commission FP7 for funding (PCATDES, Grant N.309846). IPP thanks the EPSRC for an M3S CDT (EP/L015862/1). LM and JD thank the EPSRC for funding (EP/M008754/1). Dr. Steve Firth is thanked for his assistance for our HRTEM and SEM studies. Dr. Xiaoe Li is thanked for her assistance with the preparation of the perovskite solar cell.

ABBREVIATIONS

AACVD, aerosol-assisted chemical vapor deposition; CVD, chemical vapor deposition; FE, Faradaic efficiency; HR-TEM, high-resolution transmission electron microscopy; IPCE, incident photon to current efficiency; SEM, scanning electron microscopy; SPP, solar predicted photocurrent; XPS, X-ray photoelectron spectroscopy; XRD, X-ray diffraction.

REFERENCES

(1) Broecker, W. S. Climatic Change: Are We on the Brink of a Pronounced Global Warming? *Science (80-.).* **1975**, *189*, 460–463.

(2) Gruber, N. Warming Up, Turning Sour, Losing Breath: Ocean Biogeochemistry under

Global Change. *Philos. Trans. A. Math. Phys. Eng. Sci.* **2011**, *369*, 1980–1996.

(3) Morton, O. Solar Energy: A New Day Dawning? Silicon Valley Sunrise. *Nature* **2006**, *443*, 19–22.

(4) Sovacool, B. K. The Intermittency of Wind, Solar, and Renewable Electricity Generators: Technical Barrier or Rhetorical Excuse? *Util. Policy* **2009**, *17*, 288–296.

(5) Beaudin, M.; Zareipour, H.; Schellenberglabe, A.; Rosehart, W. Energy Storage for Mitigating the Variability of Renewable Electricity Sources: An Updated Review. *Energy Sustain. Dev.* **2010**, *14*, 302–314.

(6) Tachibana, Y.; Vayssieres, L.; Durrant, J. R. Artificial Photosynthesis for Solar Water-Splitting. *Nat. Photonics* **2012**, *6*, 511–518.

(7) Fujishima, A.; Honda, K. Electrochemical Photolysis of Water at a Semiconductor Electrode. *Nature* **1972**, *238*, 37–38.

(8) Walter, M. G.; Warren, E. L.; Mckone, J. R.; Boettcher, S. W.; Mi, Q.; Santori, E. A.; Lewis, N. S. Solar Water Splitting Cells. *Chem. Rev.* **2010**, *110*, 6446.

(9) Kay, A.; Cesar, I.; Grätzel, M. New Benchmark for Water Photooxidation by Nanostructured Alpha-Fe2O3 Films. *J. Am. Chem. Soc.* **2006**, *128*, 15714–15721.

(10) Choi, S. K.; Choi, W.; Park, H. Solar Water Oxidation Using Nickel-Borate Coupled BiVO4 Photoelectrodes. *Phys. Chem. Chem. Phys.* **2013**, *15*, 6499.

(11) Yang, J.-S.; Liao, W.-P.; Wu, J.-J. Morphology and Interfacial Energetics Controls for Hierarchical Anatase/rutile TiO2 Nanostructured Array for Efficient Photoelectrochemical

Water Splitting. *ACS Appl. Mater. Interfaces* **2013**, *5*, 7425–7431.

(12) Mi, Q.; Ping, Y.; Li, Y.; Cao, B.; Brunschwig, B. S.; Khalifah, P. G.; Galli, G. A.; Gray, H. B.; Lewis, N. S. Thermally Stable N(2)-Intercalated WO(3) Photoanodes for Water Oxidation. *J. Am. Chem. Soc.* **2012**, *134*, 18318.

(13) Kim, J. K.; Shin, K.; Cho, S. M.; Lee, T.-W.; Park, J. H. Synthesis of Transparent Mesoporous Tungsten Trioxide Films with Enhanced Photoelectrochemical Response: Application to Unassisted Solar Water Splitting. *Energy Environ. Sci.* **2011**, *4*, 1465.

(14) Pesci, F. M.; Cowan, A. J.; Alexander, B. D.; Durrant, J. R.; Klug, D. R. Charge Carrier Dynamics on Mesoporous WO3 during Water Splitting. *J. Phys. Chem. Lett.* **2011**, *2*, 1900.

(15) Rao, P. M.; Cho, I, S.; Zheng, X. Flame Synthesis of WO3 Nanotubes and Nanowires for Efficient Photoelectrochemical Water-Splitting. *Proc. Combust. Inst.* **2013**, *34*, 2187.

(16) Dias, P.; Lopes, T.; Meda, L.; Andrade, L.; Mendes, A. Photoelectrochemical Water Splitting Using WO3 Photoanodes: The Substrate and Temperature Roles. *Phys. Chem. Chem. Phys.* **2016**, *18*, 5232–5243.

(17) Liu, X.; Wang, F.; Wang, Q. Nanostructure-Based WO3 Photoanodes for Photoelectrochemical Water Splitting. *Phys. Chem. Chem. Phys.* **2012**, *14*, 7894.

(18) Fabrega, C.; Murcia-Lopez, S.; Monllor-Satoca, D.; Prades, J. D.; Hernandez-Alonso, M. D.; Penelas, G.; Morante, J. R.; Andreu, T. Efficient WO3 Photoanodes Fabricated by Pulsed Laser Deposition for Photoelectrochemical Water Splitting with High Faradaic Efficiency. *Appl. Catal. B Environ.* **2016**, *189*, 133–140.

(19) Sarnowska, M.; Bienkowski, K.; Barczuk, P. J.; Solarska, R.; Augustynski, J. Highly Efficient and Stable Solar Water Splitting at (Na)WO3 Photoanodes in Acidic Electrolyte Assisted by Non-Noble Metal Oxygen Evolution Catalyst. *Adv. Energy Mater.* **2016**, *6*, 1–6.

(20) Ma, Y.; Kafizas, A.; Pendlebury, S. R.; Le Formal, F.; Durrant, J. R. Photoinduced Absorption Spectroscopy of CoPi on BiVO4: The Function of CoPi during Water Oxidation. *Adv. Funct. Mater.* **2016**, *26*, 4951–4960.

(21) Ma, Y.; Le Formal, F.; Kafizas, A.; Pendlebury, S. R.; Durrant, J. R. Efficient Suppression of Back Electron/hole Recombination in Cobalt Phosphate Surface-Modified Undoped Bismuth Vanadate Photoanodes. *J. Mater. Chem. A* **2015**, *3*, 20649.

(22) Pendlebury, S. R.; Wang, X.; Le Formal, F.; Cornuz, M.; Kafizas, A.; Tilley, S. D.; Grätzel, M.; Durrant, J. R. Ultrafast Charge Carrier Recombination and Trapping in Hematite Photoanodes under Applied Bias. *J. Am. Chem. Soc.* **2014**, *136*, 9854–9857.

(23) Zheng, J.; Sheng, W.; Zhuang, Z.; Xu, B.; Yan, Y. Universal Dependence of Hydrogen Oxidation and Evolution Reaction Activity of Platinum-Group Metals on pH and Hydrogen Binding Energy. *Sci. Adv.* **2016**, *2*, e1501602.

(24) Brillet, J.; Yum, J.-H.; Cornuz, M.; Hisatomi, T.; Solarska, R.; Augustynski, J.; Graetzel, M.; Sivula, K. Highly Efficient Water Splitting by a Dual-Absorber Tandem Cell. *Nat. Photonics* **2012**, *6*, 824–828.

(25) Saito, R.; Miseki, Y.; Sayama, K. Photoanode Characteristics of Multi-Layer Composite BiVO4 Thin Film in a Concentrated Carbonate Electrolyte Solution for Water Splitting. *J.*

Photochem. Photobiol. A Chem. **2013**, *258*, 51.

(26) Su, J.; Guo, L.; Bao, N.; Grimes, C. A. Nanostructured WO 3 /BiVO 4 Heterojunction Films for Efficient Photoelectrochemical Water Splitting. *Nano Lett.* **2011**, *11*, 1928.

(27) Rao, P. M.; Cai, L.; Liu, C.; Cho, I. S.; Lee, C. H.; Weisse, J. M.; Yang, P.; Zheng, X. Simultaneously Efficient Light Absorption and Charge Separation in WO 3 /BiVO 4 Core/Shell Nanowire Photoanode for Photoelectrochemical Water Oxidation. *Nano Lett.* **2014**, *14*, 1099–1105.

(28) Sivula, K.; Formal, F. Le; Grätzel, M. WO3−Fe2O3 Photoanodes for Water Splitting: A Host Scaffold, Guest Absorber Approach. *Chem. Mater.* **2009**, *21*, 2862–2867.

(29) Wang, W.; Dong, J.; Ye, X.; Li, Y.; Ma, Y.; Qi, L. Heterostructured TiO 2 Nanorod@Nanobowl Arrays for Efficient Photoelectrochemical Water Splitting. *Small* **2016**, *12*, 1469–1478.

(30) Choy, K. Chemical Vapour Deposition of Coatings. *Prog. Mater. Sci.* **2003**, *48*, 57.

(31) Chakrapani, V.; Thangala, J.; Sunkara, M. K. WO3 and W2N Nanowire Arrays for Photoelectrochemical Hydrogen Production. *Int. J. Hydrogen Energy* **2009**, *34*, 9050–9059.

(32) Zhang, X.; Lu, X.; Shen, Y.; Han, J.; Yuan, L.; Gong, L.; Xu, Z.; Bai, X.; Wei, M.; Tong, Y.; et al. Three-Dimensional WO3 Nanostructures on Carbon Paper: Photoelectrochemical Property and Visible Light Driven Photocatalysis. *Chem. Commun.* **2011**, *47*, 5804.

(33) Ling, M.; Blackman, C. Growth Mechanism of Planar or Nanorod Structured Tungsten

Oxide Thin Films Deposited via Aerosol Assisted Chemical Vapour Deposition (AACVD). *Phys. Status Solidi C* **2015**, *877*, 869–877.

(34) Navío, C.; Vallejos, S.; Stoycheva, T.; Llobet, E.; Correig, X.; Snyders, R.; Blackman, C.; Umek, P.; Ke, X.; Van Tendeloo, G.; et al. Gold Clusters on WO3 Nanoneedles Grown via AACVD: XPS and TEM Studies. *Mater. Chem. Phys.* **2012**, *134*, 809.

(35) Toby, B. H. EXPGUI, a Graphical User Interface for GSAS. *J. Appl. Crystallogr.* **2001**, *34*, 210–213.

(36) Casa Software Ltd http://www.casaxps.com/ (accessed Nov 21, 2016).

(37) Briggs, D.; Seah, M. P. *Practical Surface Analysis by Auger and X-Ray Photoelectron Spectroscopy*; 2nd editio.; John Wiley and Sons: Chichester, 1992.

(38) Woodward, P. M.; Sleight, A. W.; Vogt, T. Structure Refinement of Triclinic Tungsten Trioxide. *J. Phys. Chem. Solids* **1995**, *56*, 1305–1315.

(39) Nefedov, V. I.; Firsov, M. N.; Shaplygin, I. S. Electronic Structures of MRhO2, MRh2O4, RhMO4 and Rh2MO6 on the Basis of X-Ray Spectroscopy and ESCA Data. *J. Electron Spectros. Relat. Phenomena* **1982**, *26*, 65–78.

(40) Tauc, J. Optical Properties and Electronic Structure of Amorphous Ge and Si. *Mater. Res. Bull.* **1968**, *3*, 37–46.

(41) Izgorodin, A.; Izgorodina, E.; MacFarlane, D. R. Low Overpotential Water Oxidation to Hydrogen Peroxide on a MnOx Catalyst. *Energy Environ. Sci.* **2012**, *5*, 9496.

(42) Hong, S. J.; Jun, H.; Borse, P. H.; Lee, J. S. Size Effects of WO3 Nanocrystals for

Photooxidation of Water in Particulate Suspension and Photoelectrochemical Film Systems. *Int. J. Hydrogen Energy* **2009**, *34*, 3234–3242.

(43) Su, J.; Feng, X.; Sloppy, J. D.; Guo, L.; Grimes, C. A. Vertically Aligned WO3 Nanowire Arrays Grown Directly on Transparent Conducting Oxide Coated Glass: Synthesis and Photoelectrochemical Properties. *Nano Lett.* **2011**, *11*, 203–208.

(44) Heli Wang; Torbjörn Lindgren; Jianjun He; Hagfeldt, A.; Lindquist, S.-E. Photolelectrochemistry of Nanostructured WO3 Thin Film Electrodes for Water Oxidation: Mechanism of Electron Transport. *J. Phys. Chem. B* **2000**, *104*, 5686–5696.

(45) Wang, G.; Lu, X.; Li, Y. Low-Cost Nanomaterials for Photoelectrochemical Water Splitting. In *Low-cost Nanomaterials - Toward Greener and More Efficient Energy Applications*; 2014; pp. 267–295.

(46) Jin, T.; Diao, P.; Xu, D.; Wu, Q. High-Aspect-Ratio WO3 Nanoneedles Modified with Nickel-Borate for Efficient Photoelectrochemical Water Oxidation. *Electrochim. Acta* **2013**, *114*, 271–277.

(47) Lhermitte, C. R.; Garret Verwer, J.; Bartlett, B. M. Improving the Stability and Selectivity for the Oxygen-Evolution Reaction on Semiconducting WO_3 Photoelectrodes with a Solid-State FeOOH Catalyst. *J. Mater. Chem. A* **2016**, *4*, 2960–2968.

(48) Hill, J. C.; Choi, K. Effect of Electrolytes on the Selectivity and Stability of N-Type WO3 Photoelectrodes for Use in Solar Water Oxidation. *J. Phys. Chem. C* **2012**, *116*, 7612–7620.

(49) Pihosh, Y.; Turkevych, I.; Mawatari, K.; Uemura, J.; Kazoe, Y.; Kosar, S.; Makita, K.;

Sugaya, T.; Matsui, T.; Fujita, D.; et al. Photocatalytic Generation of Hydrogen by Core-Shell WO3/BiVO4 Nanorods with Ultimate Water Splitting Efficiency. *Sci. Rep.* **2015**, *5*, 11141.

(50) Mi, Q.; Zhanaidarova, A.; Brunschwig, B. S.; Gray, H. B.; Lewis, N. S. No Title. *Energy Environ. Sci.* **2012**, *5*, 5694−5700.

(51) Seabold, J.; Choi, K.-S. No Title. *Chem. Mater.* **2011**, *23*, 1105−1112.

(52) Bryant, D.; Aristidou, N.; Pont, S.; Sanchez-Molina, I.; Chotchunangatchaval, T.; Wheeler, S.; Durrant, J. R.; Haque, S. A. Light and Oxygen Induced Degradation Limits the Operational Stability of Methylammonium Lead Triiodide Perovskite Solar Cells. *Energy Environ. Sci.* **2016**, *9*, 1655–1660.

(53) Chen, Y.-S.; Manser, J. S.; Kamat, P. V. All Solution-Processed Lead Halide Perovskite-BiVO4 Tandem Assembly for Photolytic Solar Fuels Production. *J. Am. Chem. Soc.* **2015**, *137*, 974–981.

SYNOPSIS: Solar water splitting is a promising solution for the renewable production of hydrogen as an energy vector. Nanostructured photoelectrodes show the highest water splitting efficiencies, but lack scalable routes for commercial scale-up. Here we report a direct and scalable route to the single step fabrication of WO_3 nano-needle structure photoanodes. When coupled with a photovoltaic device, we predict a solar-to-hydrogen efficiency of *ca* 1 %.

TOC graphic:

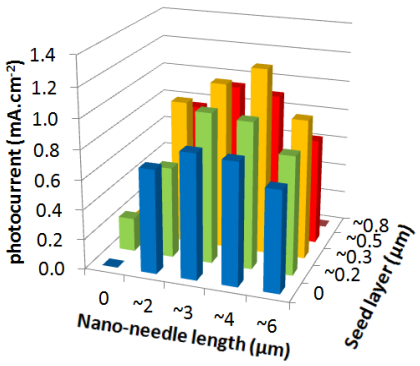
photocurrent (mA.cm-2)
1.4
1.2
1.0
0.8
0.6
0.4
0.2
0.0
0
~2
~3
~4
~6
Nano-needle length (µm)
0
~0.2
~0.3
~0.5
~0.8
Seed layer (µm)